

A Neuroevolution Potential for Gallium Oxide: Accurate and Efficient Modeling of Polymorphism and Swift Heavy-Ion Irradiation

Yaohui Gu,^{1, 2} Binbo Li,^{1, 2, *} Linyang Jiang,^{1, 2} Yuhui Hu,^{1, 2, 3} Wenqiang Liu,^{1, 2} Lijun Xu,^{1, 2} Pengfei Zhai,^{1, 2} Jie Liu,^{1, 2} and Jinglai Duan^{1, 2, 4, †}

¹*State Key Laboratory of Heavy Ion Science and Technology,*

Institute of Modern Physics, Chinese Academy of Sciences, Lanzhou 730000, China

²*School of Nuclear Science and Technology, University of Chinese Academy of Sciences, Beijing 100049, China*

³*School of Materials & Energy, Lanzhou University, Lanzhou, 730000, China*

⁴*Advanced Energy Science and Technology Guangdong Laboratory, Huizhou 516000, China*

(Dated: January 16, 2026)

Gallium oxide (Ga_2O_3) is a wide-bandgap semiconductor with promising applications in high-power and high-frequency electronics. However, its complex polymorphic nature poses substantial challenges for fundamental studies, particularly in understanding phase-transformation behaviors under nonequilibrium conditions. Here, we develop a robust, accurate, and computationally efficient machine-learning interatomic potential (MLIP) for Ga_2O_3 based on the neuroevolution potential (NEP) framework combined with an energy-dependent weighting strategy. The resulting NEP potential demonstrates clear advantages over the state-of-the-art tabGAP potential with respect to both accuracy and computational efficiency. Furthermore, we introduce a physically process-oriented sampling strategy to systematically augment the training dataset, thereby enhancing the MLIP performance for targeted physical phenomena. As a representative application, a dedicated NEP potential is constructed for swift heavy-ion (SHI) irradiation simulations of $\beta\text{-Ga}_2\text{O}_3$. The simulated results are in quantitative agreement with experimental observations and provide a consistent physical explanation for the reported experimental discrepancies regarding phase transformations in the ion track of $\beta\text{-Ga}_2\text{O}_3$.

I. INTRODUCTION

Gallium oxide (Ga_2O_3), a representative of the fourth generation of semiconductors, has garnered widespread interest due to its unique physical and electronic properties [1]. With an ultra-wide bandgap, high breakdown electric field, and transparency in the deep ultraviolet region, Ga_2O_3 holds significant promise for applications including power electronics [2], solar-blind UV photodetectors [3], and gas sensors [4]. In addition to its thermodynamically stable monoclinic β phase, Ga_2O_3 exhibits a rich polymorphism, including metastable α (corundum-type), γ (defective spinel), δ (bixbyite), and κ (orthorhombic) phases [5]. This polymorphic diversity opens new avenues for directional material design and property tuning but also presents formidable challenges in controlled synthesis, phase stability, and interface engineering. Consequently, a comprehensive theoretical understanding of Ga_2O_3 —particularly of its complex polymorphic nature—is essential for realizing its full potential in practical applications.

Early theoretical investigations of Ga_2O_3 focused on its electronic structure using first-principles methods [5–7], laying the groundwork for understanding its doping behavior [8], lattice dynamics [9, 10], interface states [11], and phase stability [12]. While first-principles approaches continue to offer critical insights, their high

computational cost and limited scalability pose significant challenges for modeling large-scale phenomena, such as irradiation-induced phase transitions or extended defect evolution [13, 14]. Conversely, molecular dynamics (MD) enables simulations at larger time and length scales; however, the empirical interatomic potentials it relies on often struggle to accurately capture the complex potential energy landscape of Ga_2O_3 ’s polymorphic phases [15].

In recent years, the rapid advancement of artificial intelligence has ushered in a paradigm shift in materials science [16]. Among the most transformative developments is the emergence of machine learning interatomic potentials (MLIPs), which offer near-DFT accuracy combined with excellent scalability, making them powerful alternatives to traditional empirical potentials in MD simulations [17]. Motivated by these advantages, several pioneering research groups have made continuous efforts to develop MLIPs tailored for Ga_2O_3 , spanning a wide range of polymorphic phases—from the thermodynamically stable β phase [18–20] to metastable α [21], κ [22], ϵ [21], and amorphous configurations [23]. A landmark achievement was realized by Zhao *et al.* [24], who introduced a general-purpose MLIP referred to as tabGAP, aiming to accurately describe the atomic interactions across all major Ga_2O_3 polymorphs. This potential has enabled large-scale simulations of defect evolution [25–27], phase transformations [28], and crystallization dynamics [29, 30], and has played a pivotal role in recent studies of irradiation effects in Ga_2O_3 [31–34]. However, despite its considerable success, tabGAP still exhibits notable limitations compared to other state-of-

* Y.G. and B.L. contributed equally to this work.

† Corresponding author. Email: j.duan@impcas.ac.cn

the-art MLIPs, including relatively lower accuracy and computational speed, as will be demonstrated in the following sections. These limitations motivate us to rigorously benchmark the overall performance of tabGAP and develop a new, more accurate and efficient MLIP for Ga_2O_3 .

In this work, we adopt the neuroevolution potential (NEP) framework, which is well known for its high computational efficiency [35], to construct MLIPs for Ga_2O_3 . To capture the complex potential-energy landscape of Ga–O compounds, we propose an energy-dependent weighting strategy for training. With this strategy, the resulting NEP model achieves consistently higher prediction accuracy than tabGAP across all energy ranges and for most configuration types. Furthermore, we find that both MLIP architectures exhibit varying degrees of zero-shot prediction limitations as well as systematic softening of the energy landscape. To mitigate these issues, we further augment the training dataset with additional configurations generated following physically motivated sampling rules. As a representative application, to clarify recent controversies surrounding swift heavy-ion (SHI) irradiation experiments on β - Ga_2O_3 , we train a dedicated NEP model using a dataset augmented with additional γ -phase configurations and β -phase heating–cooling pathways. High-throughput MD simulations based on this model yield a series of irradiated β - Ga_2O_3 structures across a wide range of electronic energy losses. The simulated results are in quantitative agreement with experimental observations and provide a consistent physical explanation for the reported experimental discrepancies.

II. METHODOLOGY

A. NEP architecture

NEP, developed by Fan *et al.*, consists of an ACE-like descriptor constructed using Chebyshev polynomials and a regression model based on a feedforward neural network [36–38]. Its explicit atomic-environment featurization is carefully designed to strike an excellent balance between prediction accuracy and computational efficiency. Moreover, NEP is natively implemented in the Graphics Processing Units Molecular Dynamics (GPUMD) package, enabling an impressive computational throughput of up to 1×10^7 atom-steps per second on a single GPU [35]. Considering its overall performance, NEP stands out as one of the most promising MLIPs for large-scale simulations of Ga_2O_3 under a wide range of physical conditions.

The radial function $g_n(r_{ij})$, which serves as the basic building block of the NEP descriptor, is defined as

$$g_n(r_{ij}) = \sum_k c_{nk}^{ij} f_k(r_{ij}), \quad (1)$$

where r_{ij} is the distance between atoms i and j , c_{nk}^{ij} is a trainable parameter, and $f_k(r_{ij})$ is a Chebyshev-based

radial basis function with a finite cutoff:

$$f_k(r_{ij}) = \frac{1}{2} [T_k(2(r_{ij}/r_{\text{cut}} - 1)^2 - 1) + 1] s_c(r_{ij}), \quad (2)$$

where $T_k(x)$ is the k -th-order Chebyshev polynomial of the first kind, and $s_c(r_{ij})$ is a cutoff function

$$s_c(r_{ij}) = \begin{cases} \frac{1}{2}[1 + \cos(\pi r_{ij}/r_{\text{cut}})], & r_{ij} \leq r_{\text{cut}}, \\ 0, & r_{ij} > r_{\text{cut}}. \end{cases} \quad (3)$$

The n -th radial descriptor of atom i is then constructed as

$$q_n^i = \sum_{j \neq i} g_n(r_{ij}), \quad (4)$$

and the n -th angular descriptor of atom i with angular-momentum index l is defined as

$$q_{n,l}^i = \sum_{j \neq i} \sum_{k \neq i} g_n(r_{ij}) g_n(r_{ik}) P_l(\theta_{ijk}), \quad (5)$$

where $P_l(\theta_{ijk})$ is the l -th-order Legendre polynomial of the angle θ_{ijk} between atoms i , j , and k .

All descriptors are concatenated into a single vector, which is then passed through a feedforward neural network to predict the atomic potential energy:

$$U^i = \sum_{\mu=1}^{N_{\text{neu}}} \omega_{\mu}^{(1)} \tanh \left(\sum_{\nu=1}^{N_{\text{des}}} \omega_{\mu\nu}^{(0)} q_{\nu}^i - b_{\mu}^{(0)} \right) - b^{(1)}, \quad (6)$$

where N_{neu} is the number of neurons in the hidden layer, N_{des} is the number of descriptors, $\omega_{\mu}^{(1)}$ and $b^{(1)}$ are the output-layer weight and bias, $\omega_{\mu\nu}^{(0)}$ and $b_{\mu}^{(0)}$ are the hidden-layer weights and biases, and q_{ν}^i denotes the ν -th descriptor of atom i .

B. Hyperparameters

In this work, we use the fourth generation of NEP [38] to construct the MLIP for Ga_2O_3 . To faithfully capture the complex potential energy landscape of Ga_2O_3 , we adopt a relatively large parameterization strategy. Specifically, 9 radial descriptors ($r_{\text{cut}} = 6 \text{ \AA}$) and 42 angular descriptors ($r_{\text{cut}} = 4 \text{ \AA}$) are employed, with a single hidden layer containing 100 neurons. The maximum Chebyshev polynomial orders are set to 12 and 10 for the radial and angular descriptors, respectively. In addition, 4-body and 5-body angular terms are included as described in Ref. [37]. In total, the resulting model contains 11,377 trainable parameters. We also tested larger parameter settings; however, they did not provide noticeable improvements in accuracy while causing a substantial increase in computational cost.

A robust training-weighting scheme is needed to balance the accuracy across distinct atomic environments, which is essential for achieving successful training over an

extremely wide range of average atomic energies, spanning from the most stable β phase to highly unstable, nonstoichiometric amorphous states under high pressure. Two distinct training strategies are tested in this work. The first strategy is to adopt the phase-dependent scaling scheme proposed in Ref. [24], which enhances the descriptive capability of the model for key Ga_2O_3 phases, including its metastable crystalline structures. The second strategy is to scale the training weights of all configurations according to their average potential energy per atom, ensuring that the NEP model primarily focuses on low-energy configurations while still retaining reasonable descriptive capability for high-energy states. The scaling factor \mathcal{S} is defined as

$$\mathcal{S} = \frac{1}{|e_i/\epsilon - e_{\beta\text{-phase}}/\epsilon|^\alpha + 1}, \quad (7)$$

where e_i is the average potential energy per atom of the i -th configuration, $e_{\beta\text{-phase}}$ denotes that of the β phase, and α and ϵ are small constants controlling the strength of the scaling.

The average energy, atomic forces, and virial of each training configuration are used as training targets, with global weights of $\lambda_e = \lambda_f = \lambda_v = 1$, following Ref. [39]. Both \mathcal{L}_1 and \mathcal{L}_2 regularizations are applied with $\lambda_1 = \lambda_2 = 0.05$ to avoid overfitting [37].

C. Datasets

The dataset reported in Ref. [24], which was originally used to construct soapGAP and tabGAP models for Ga_2O_3 and is hereafter referred to as the GAP dataset, serves as the main part of our training set. The GAP dataset contains 1,630 configurations covering a wide range of Ga–O systems, from crystalline Ga_2O_3 to nonstoichiometric, amorphous, and molten states, and also includes a number of few-atom systems for calibration. This dataset provides a rich collection of representative atomic configurations, although with a relatively limited number of samples. It is generally sufficient for broad, general-purpose applications where ultimate accuracy is not the primary concern.

However, the GAP dataset lacks certain key configurations required to recover essential physical features in our irradiation simulations. To address this issue, we augment the dataset with additional training configurations generated using exactly the same sampling protocol as for the GAP dataset. These newly sampled configurations are found to lie beyond the extrapolation capability of tabGAP and are crucial for accurately capturing SHI irradiation-induced phenomena. Two types of configurations are added. The first type comprises 60 structures along the energy–volume equation-of-state curve of the γ phase. This addition is motivated by the fact that the $\beta \rightarrow \gamma$ transition is widely observed in radiation experiments on Ga_2O_3 [32–34], yet γ -phase configurations are underrepresented in the original GAP dataset.

The second type consists of 300 configurations sampled from heating–cooling processes of the β phase under various pressure and volume conditions, because such thermodynamic pathways frequently occur during irradiation. Our principle component analysis (PCA) shows that these newly added configurations effectively fill the gap in the configuration space with the β phase and the molten/amorphous states that exists in the original GAP dataset [Fig. 6(d)].

D. Simulations

The SHI irradiation simulations are performed using the GPUMD package [35], following the strategy proposed in Ref. [40]. In general, the simulations proceed as follows. (1) The energy deposition from SHIs in Ga_2O_3 is simulated using TREKIS, a Monte Carlo code developed to model the electronic kinetics following SHI impact on matter [41, 42]. (2) The resulting radial energy profile of the ion track is used to initialize the atomic velocities of the Ga_2O_3 lattice for subsequent MD simulations, with a conversion factor of 0.45 applied to reproduce the experimentally observed track dimensions. (3) The MD simulations are carried out in the NVE ensemble, while the boundary temperature is controlled using Nose-Hoover chain thermostats, with the coupling parameter tuned to 1,000. Further methodological details regarding TREKIS are provided in Appendix A, and technical details for MD simulations are provided in Appendix B.

To ensure a fair comparison, all prediction tests for both NEP and tabGAP are performed using the same LAMMPS installation and hardware, eliminating potential software- and hardware-related biases.

III. RESULTS AND DISCUSSION

A. Overall performance comparison

A comprehensive comparison of the predictive capabilities of NEP and tabGAP is shown in Fig. 1 with results summarized in Table I. Our NEP model, trained with the energy-dependent weighting strategy, exhibits consistently superior performance over tabGAP. Given the wide energy span of the original GAP dataset, we separately analyze (1) configurations spanning a broad energy range up to 5 eV/atom above the β phase (91.5% of the dataset) and (2) relatively stable configurations within 0.5 eV/atom above the β phase (45.3% of the dataset).

For the configurations with a broad energy range, NEP offers pronounced accuracy improvements in predicting energies [Fig. 1(a)], forces [Fig. 1(c)], and virials [Fig. 1(e)] compared with tabGAP. Specifically, the mean absolute error (MAE) of the energy predicted by NEP is 16.4 meV/atom, about one third of that of tabGAP (48.3 meV/atom). Moreover, the root mean square error (RMSE) of energy predicted by tabGAP reaches

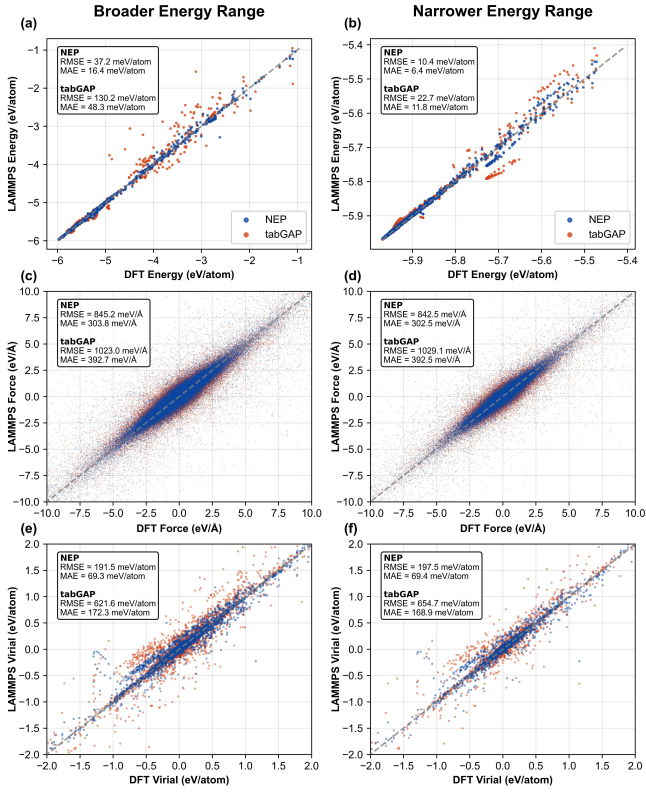


Figure 1. Detailed comparison of the prediction accuracy of the NEP and tabGAP models. Blue and red dots represent NEP and tabGAP results, respectively. Panels (a), (c), and (e) show the predicted energies, forces, and virials of the GAP-dataset configurations with average energies ranging from -5.9 to -0.9 eV/atom. Panels (b), (d), and (f) present the corresponding results for a narrower energy window from -5.9 to -5.4 eV/atom.

130.2 meV/atom, which is 3.5 times higher than that of NEP (37.2 meV/atom), indicating a potential instability of tabGAP over the wide energy range. The MAE of force prediction by NEP is 303.9 meV/Å, approximately three quarters of that of tabGAP (392.7 meV/Å), while the MAE of virial prediction is 69.3 meV/atom for NEP and 172.3 meV/atom for tabGAP. The overall MAEs of both models remain relatively large mainly because the dataset covers an extremely broad energy range. For the relatively stable configurations, both models show significant improvements in energy prediction [Fig. 1(b)], whereas the improvements in force [Fig. 1(d)] and virial [Fig. 1(f)] predictions are less pronounced. The MAE of energy prediction by NEP is 6.4 meV/atom, about half of that of tabGAP (11.8 meV/atom), and NEP still maintains noticeable advantages in force and virial predictions.

Beyond its superior prediction accuracy, NEP also demonstrates significantly higher computational throughput than tabGAP, breaking the accuracy-efficiency trade-off common in modern MLIP architec-

Table I. Prediction accuracy comparison between tabGAP and NEP for configurations with broader (up to 5 eV/atom above β phase) and narrower (up to 0.5 eV/atom above β phase) energy ranges. Energy values are in meV/atom, force values are in meV/Å, and virial values are in meV/atom.

Model	Energy		Force		Virial	
	MAE	RMSE	MAE	RMSE	MAE	RMSE
tabGAP (Broader)	48.3	130.2	392.7	1023.0	172.3	621.6
NEP (Broader)	16.4	37.2	303.8	845.2	69.3	191.5
tabGAP (Narrower)	11.8	22.7	392.5	1029.1	168.9	654.7
NEP (Narrower)	6.4	10.4	302.5	842.5	69.4	197.5

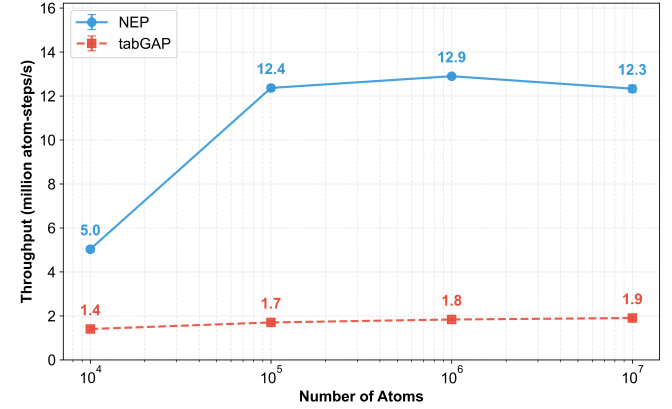


Figure 2. Comparison of the computational throughput between NEP and tabGAP for systems of different sizes. The throughput of NEP is measured on a single NVIDIA H100 GPU, while that of tabGAP is measured on eight CPU nodes, each equipped with two 24-core Intel Xeon Gold 6240R processors.

tures. As shown in Fig. 2, we benchmarked the computational throughput of NEP and tabGAP for systems containing between 10^4 and 10^7 atoms, and found that NEP consistently achieves significantly higher throughput across all system sizes. For the relatively small system size of 10^4 atoms, NEP reaches a throughput of approximately 5×10^6 atom-steps per second, which is about four times higher than that of tabGAP (1.4×10^6 atom-steps per second). As the system size increases beyond 10^5 atoms, the throughput of NEP rapidly converges to around 1.25×10^7 atom-steps per second, whereas the throughput of tabGAP encounters a clear bottleneck at approximately 2×10^6 atom-steps per second under our test conditions. It is worth noting that the two potentials are benchmarked on different hardware platforms: NEP is evaluated on a single NVIDIA H100 GPU, while tabGAP is tested on eight CPU nodes, each equipped with two 24-core Intel Xeon Gold 6240R processors. Nevertheless, we believe that this comparison remains meaningful, as both hardware platforms have been independently benchmarked by our group and exhibit comparable peak double-precision floating-point performance, with the H100 GPU reaching 18.27 TFLOPS and the

eight CPU nodes achieving 18.92 TFLOPS.

To elucidate the origins of this performance advantage, we systematically compared the prediction errors of NEP and tabGAP across all 22 configuration types in the GAP dataset [Fig. 3]. We find that the energy MAE of tabGAP exhibits strong fluctuations among different configuration types, with some types showing very small errors below 3 meV/atom (e.g., β phase, δ phase, hex* phase, and GaO_3), while others display much larger errors exceeding 50 meV/atom (e.g., dimers, trimers, O clusters, and various nonstoichiometric structures). This fluctuation is a direct consequence of the configuration-type weighting strategy adopted in tabGAP, which assigns higher weights to crystalline phases of Ga_2O_3 [24]. However, this strategy assigns identical weights to configurations that possess very different average energies, as illustrated in Fig. 4(a). For example, a β -phase crystal cell equilibrated at ambient conditions is assigned the same weight as a β -phase crystal cell compressed to about 60% of its lattice constant, even though their average energies differ by \sim 50 eV/atom. From a thermodynamic perspective, configurations with higher average energies correspond to significantly lower occurrence probabilities, whereas the configuration-type weighting strategy treats them equally.

In contrast, the NEP model demonstrates more consistent energy prediction accuracy across different configuration types. As shown in Fig. 3, the NEP model trained with our energy-dependent weighting strategy substantially reduces the MAE for nonstoichiometric and amorphous configurations while maintaining low MAE values for crystalline phases. As a result, NEP achieves a markedly improved overall energy-prediction accuracy compared with tabGAP across different energy ranges [Fig. 4(b)]. Moreover, the improvement in force predictions achieved by NEP over tabGAP is less dramatic but more uniform across different configuration types [Fig. 3(b)]. For noncrystalline configurations, the force MAE of NEP is consistently slightly smaller than that of tabGAP, whereas for crystalline configurations the performances of the two models are largely comparable. Notably, the improvement in virial prediction is the most pronounced [Fig. 3(c)]. For noncrystalline configurations, the virial MAE of NEP is significantly smaller than that of tabGAP, and for crystalline configurations NEP also consistently yields smaller errors.

We believe that the overall superior performance of NEP over tabGAP in predicting energies, forces, and virials is primarily attributed to our energy-dependent weighting strategy, as illustrated in Fig. 4(a). The weighting factors remain close to unity for the most stable configurations, decrease to 1/2 when the average potential energy increases by 1 eV/atom above that of the optimized β phase, and then rapidly drop with increasing energy, eventually becoming smaller than 0.02 for the highest-energy configurations in the GAP dataset. The energy-prediction performances of tabGAP, NEP trained with energy-dependent weighting, and NEP trained with

configuration-type weighting over different energy ranges are shown in Fig. 4(b). With configuration-type weighting, NEP outperforms tabGAP only for configurations whose average energies exceed those of the optimized β phase by more than 0.5 eV/atom. In contrast, with the energy-dependent weighting scheme, NEP surpasses tabGAP across the entire energy range, at the cost of only a decrease in accuracy for thermodynamically rare high-energy configurations.

B. Training set augmentation

The $\beta \rightarrow \gamma$ transition is a key phenomenon widely observed in irradiation experiments on Ga_2O_3 [32–34]. However, γ -phase configurations are underrepresented in the original GAP dataset, raising concerns about whether tabGAP can accurately describe the physical properties of the γ phase. To address this issue, we sampled 60 configurations along the energy–volume curve of the γ phase using the same sampling protocol as employed for the GAP dataset. The energy–volume curve of the γ phase obtained from DFT calculations, together with the corresponding curves of the α , β , δ , and κ phases included in the original GAP dataset, are used as reference data in Fig. 5 to assess the performance of NEP (on the augmented dataset) and tabGAP in describing the equation of state of Ga_2O_3 polymorphs.

The first notable observation is that tabGAP systematically overpredicts the energy of the γ phase by nearly 20 meV/atom relative to the DFT results, indicating limited extrapolation capability for zero-shot configurations that deviate from its training set. NEP shows improved zero-shot performance for γ -phase configurations [Fig. S1], although it still overestimates their energies. The NEP model trained with the augmented dataset performs best, achieving an energy MAE about 3 meV/atom for the γ phase. In addition, both NEP and tabGAP accurately reproduce the energy–volume curves of the α and β phases, with predictions nearly overlapping with the DFT data. These two phases are the most extensively studied polymorphs in the Ga_2O_3 community, and their accurate equation-of-state description is therefore essential for the overall reliability of MLIPs. Notably, NEP also provides a good description of the κ -phase energy–volume curve, whereas tabGAP exhibits a noticeable overestimation of the corresponding energies. Given that the $\beta \rightarrow \kappa$ transition has also been reported in irradiation experiments on Ga_2O_3 [33], the improved description of the κ phase constitutes another advantage of NEP over tabGAP.

Although NEP performs better for most polymorphs, tabGAP shows a clear advantage in describing the δ phase. However, it is worth noting that both the δ and γ phases are metastable structures that possess similar cohesive energies despite their different densities. As a result, although NEP slightly overpredicts the energies of both δ and γ phases by about 3 meV/atom, it still

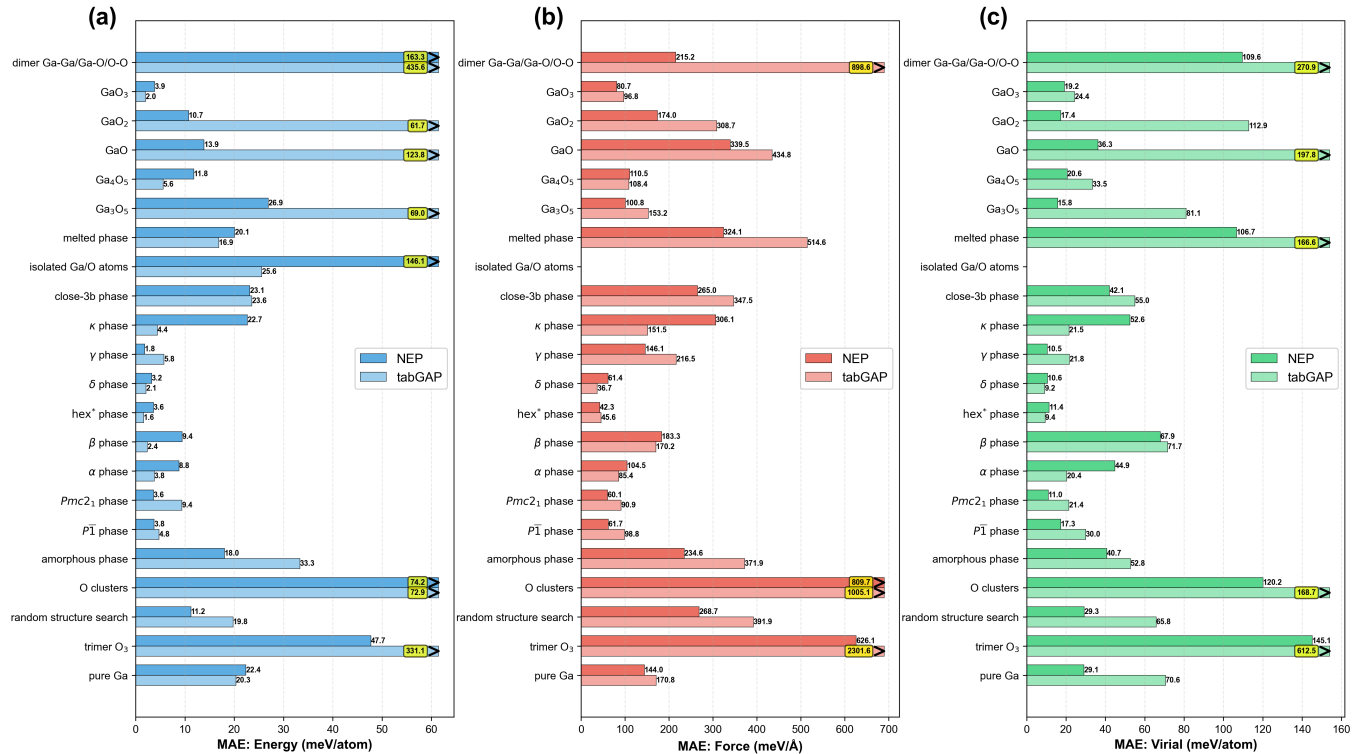


Figure 3. Comparison of the MAE of (a) energy, (b) force, and (c) virial predictions by NEP and tabGAP for different config types in the GAP dataset.

correctly captures their relative energetics and thermodynamic similarity. In contrast, the accurate description of the δ phase but the substantial overprediction of the γ phase by tabGAP suggest that tabGAP may fail to reproduce the thermodynamic proximity between the δ and γ phases.

Irradiation of solids is often accompanied by atomic recoil and/or electronic excitation processes, which can give rise to pronounced local thermal effects. As a consequence, melting, cooling, and subsequent recrystallization processes are frequently observed during irradiation. Whether an MLIP can reliably describe such highly non-equilibrium processes is therefore crucial for irradiation simulations. Moreover, the disordered structures generated during heating exhibit a much more complex potential-energy landscape than the original crystalline phases, posing significant challenges to both the completeness of the training dataset and the zero-shot capability of MLIPs.

To systematically assess the performance of NEP and tabGAP in describing the heating–cooling behavior of the β phase, we sampled 600 configurations from six independent MD simulations. These simulations employed a NEP model trained on the original GAP dataset to perform heating–cooling cycles on a 160-atom β -phase supercell, with temperatures varying between 800 K and 4000 K. Six distinct simulation conditions were considered:

- (1) Config 0GPa: NPT at 0 GPa;
- (2) Config 1GPa: NPT at 1 GPa;
- (3) Config 10GPa: NPT at 10 GPa;
- (4) Config v1: NVT at the original cell volume;
- (5) Config v0.9: NVT with the volume rescaled to 0.9;
- (6) Config v1.1: NVT with the volume rescaled to 1.1.

The energy predictions obtained using tabGAP and the NEP model trained on the GAP dataset are compared with the corresponding DFT reference data in Fig. 6(a) and Fig. 6(b), respectively. Overall, NEP exhibits better zero-shot performance for low-energy configurations than tabGAP, whereas both models systematically underpredict the energies of high-energy configurations. Specifically, tabGAP overestimates the energies of the low-energy configurations in Figs. 0GPa, 1GPa, and v1.1, indicating an overall energy overestimation for configurations corresponding to relatively low environmental pressures near the melting temperature. In contrast, NEP consistently provides more accurate predictions for the low-energy configurations, further demonstrating its superior extrapolation capability. For the high-energy configurations, both models exhibit systematic softening issues [43], characterized by an overall underprediction of the energies of configurations far from equilibrium. This softening behavior is more pronounced for NEP than for tabGAP, resulting in an overall MAE of 17.4 meV/atom in Fig. 6(b), slightly larger than that of tabGAP (16.5 meV/atom) shown in Fig. 6(a).

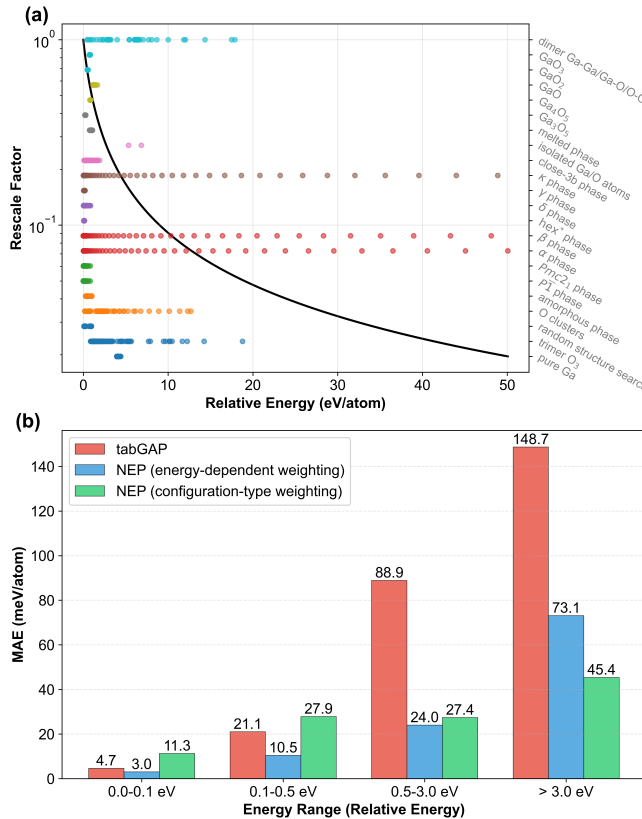


Figure 4. (a) Illustration of the energy-dependent weighting strategy, where the black curve represents the rescaling factor as a function of the average potential energy. All samples in the GAP dataset are shown as dots colored according to their configuration types; their positions along the horizontal axis indicate their average potential energies. (b) Comparison of the energy-prediction performance of tabGAP, NEP with energy-dependent weighting, and NEP with configuration-type weighting over different energy ranges.

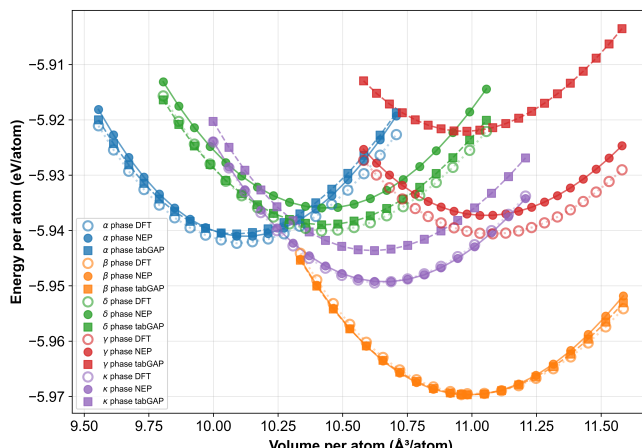


Figure 5. Energy-volume curves for the α , β , δ , γ , and κ phases predicted by NEP (solid circles) and tabGAP (solid squares), compared with DFT reference data (open circles). Different phases are color-coded as indicated.

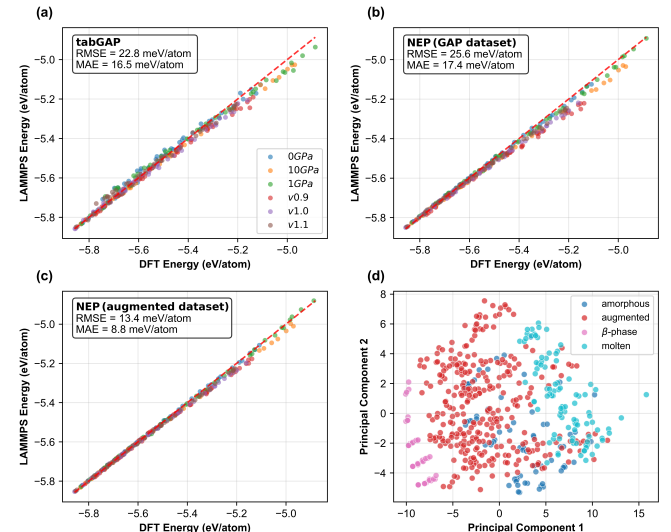


Figure 6. Energy predictions for configurations sampled from heating–cooling processes of the β phase under various pressure and volume conditions, as predicted by (a) tabGAP, (b) NEP trained on the GAP dataset, and (c) NEP trained on the augmented dataset. (d) PCA projection of configurations from the heating–cooling processes along with related configurations from the GAP dataset.

To alleviate the softening problem of NEP, half of these 600 configurations were selected based on PCA filtering [44] and added to the augmented training dataset. As shown in Fig. 6(c), the NEP model trained on the augmented dataset exhibits significantly improved performance across the entire energy range. The overall MAE is reduced to 8.8 meV/atom, which is approximately half of that obtained with models trained on the original GAP dataset. Although the softening problem is not completely eliminated, this is a reasonable compromise by the energy-dependent weighting strategy, as the primary objective of our NEP training is to accurately describe stable and metastable states under ambient conditions. Figure 6(d) presents the PCA projection of the training configurations from the heating–cooling processes together with related configurations from the GAP dataset. The newly added samples effectively fill the gaps in descriptor space between the original β -phase, molten, and amorphous configurations, thereby validating our sampling strategy.

C. SHI irradiation simulations

Recently, SHI irradiation experiments on β -Ga₂O₃ have been carried out by three independent groups [33, 34, 45, 46]. However, these studies have reported notably different conclusions regarding the resulting track structures. Xu *et al.* [45] reported that the tracks are fully amorphous when the electronic energy loss (S_e) exceeds a threshold of approximately 17 keV/nm. In con-

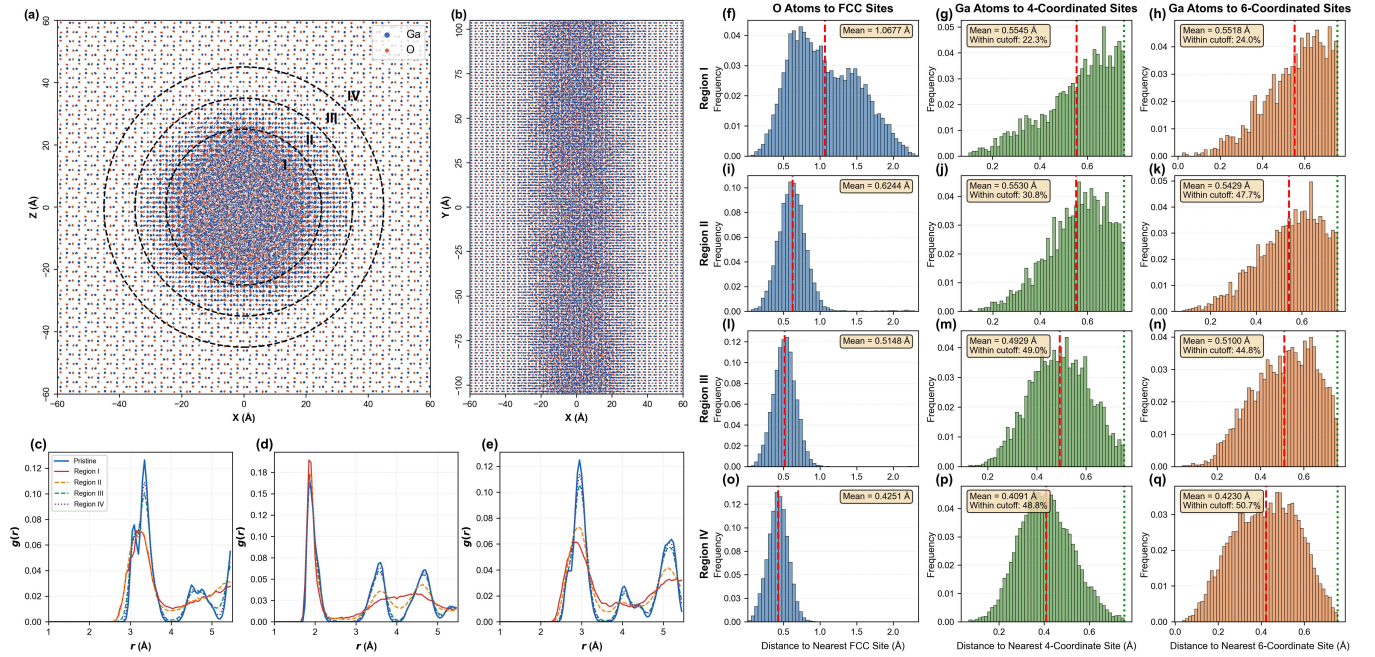


Figure 7. Analysis of a representative ion track in β -Ga₂O₃ generated by the energy deposition from a 70 MeV ^{181}Ta ion. (a) Transverse and (b) longitudinal cross-sectional views of the SHI-irradiated β -Ga₂O₃ atomic structure. Four distinct regions are identified in the transverse view (from center to periphery): amorphous core (region I), γ phase (region II), deformed β phase (region III), and pristine β phase (region IV). (c) Radial distribution functions for each region. (d) Atomic-displacement distributions relative to the ideal β -phase lattice sites for each region.

trast, Han *et al.* [33] observed the formation of γ , δ , and κ phases within the tracks. Abdullaev *et al.* [34] further reported that the tracks in β -Ga₂O₃ are nearly pure γ phase at S_e of approximately 21 keV/nm. To clarify these experimental discrepancies, reliable theoretical simulations of SHI irradiation in β -Ga₂O₃ are highly desirable. Although several related MD simulations based on tabGAP potentials have been reported [33, 34], the limitations of tabGAP discussed above raise concerns regarding the reliability of its predictions for track structures. Therefore, we performed SHI irradiation simulations on β -Ga₂O₃ using the NEP model trained on the augmented dataset with energy-dependent weighting, with the aim of demonstrating the practical predictive capability of NEP by elucidating the experimental discrepancies.

A representative ion track formed in β -Ga₂O₃ and the corresponding structural analysis are shown in Fig. 7. The ion track is generated by MD simulations driven by the energy deposition of a 70 MeV ^{181}Ta ion ($S_e = 26.05$ keV/nm in TREKIS), with a total simulation time of 200 ps. Based on the transverse cross-sectional view [Fig. 7(a)], the atomic configuration is manually divided into four concentric regions from the center to the periphery: the amorphous core (region I), the γ phase (region II), a deformed β phase (region III), and the pristine β phase (region IV). Figure 7(c) presents the radial distribution functions (RDFs) for each region, while Fig. 7(d) shows the distributions of atomic displacements with respect to the ideal β -phase lattice sites; together,

these analyses are used to assist structural identification. More conventional crystalline-structure analysis methods are not adopted here because the atomic structure of the γ phase remains highly disordered and is not uniquely defined [47]. Although the γ -Ga₂O₃ phase is commonly associated with a defect-spinel structure, it can be more naturally interpreted as a disordered form of β -Ga₂O₃ [48]. Importantly, during the $\beta \rightarrow \gamma$ transition, the oxygen sublattice remains largely preserved. This allows the oxygen lattice of β -Ga₂O₃ to be used as a common reference framework for structural analysis. From this perspective, gallium atoms are expected to occupy the four- and six-coordinated sites of the oxygen sublattice in both the β and γ phases, while the relative population of these coordination environments differs between the two phases. Therefore, the combined use of RDFs and atomic-displacement distributions provides a robust and physically meaningful approach for identifying the structural characteristics within the ion track.

Both amorphous core and γ -phase shell manifests high-contrast regions in transmission electron microscopy (TEM) experiments, with a diameter of approximately 5.9 nm, consistent with the TEM measurements reported in Ref. [45]. In the core region, the RDFs are characterized by a solitary nearest-neighbor peak, with the absence of long-range structural features confirming the transition to a disordered state. The atomic-displacement distributions further reveal that oxygen atoms completely leave their original fcc sites, and most gallium atoms are

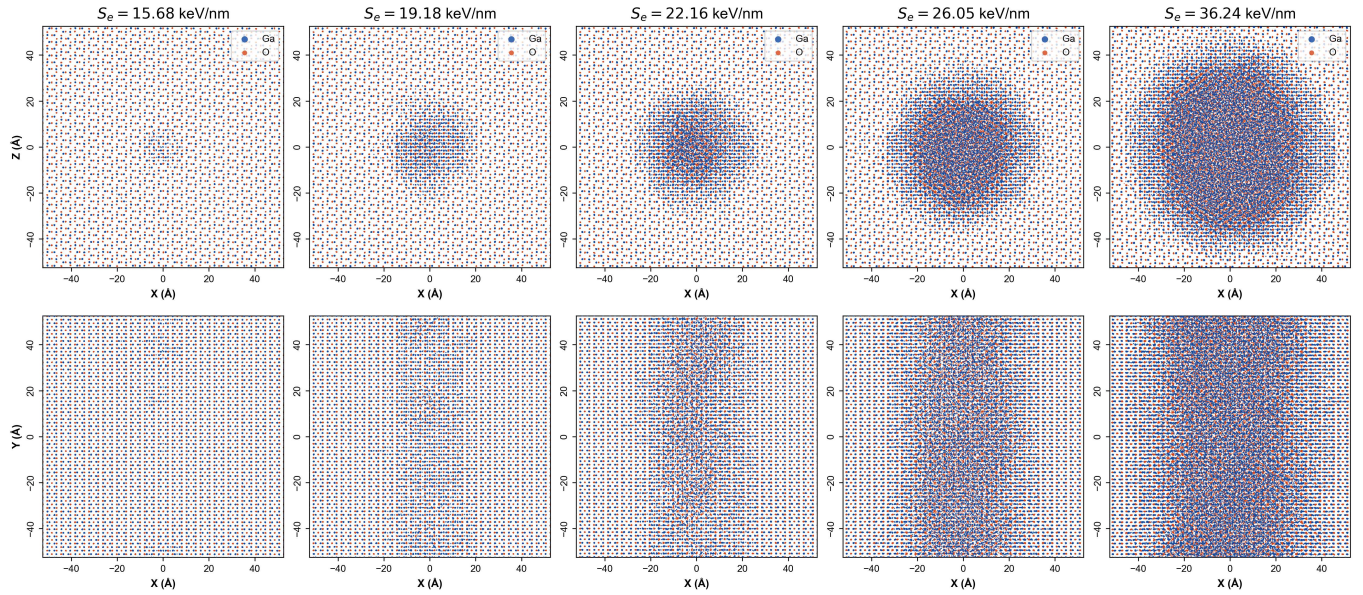


Figure 8. Transverse and longitudinal cross-sectional views of the SHI-irradiated β - Ga_2O_3 atomic structure with various electronic energy losses.

also displaced away from the vicinity of their original four- and six-coordinated sites. Outside the amorphous core, a clear γ -phase shell is observed. In this region, gallium atoms are randomly distributed among four- and six-coordinated sites, while oxygen atoms predominantly occupy their pristine fcc positions. The RDF analysis shows the absence of the second gallium–gallium peak, whereas the characteristic fcc oxygen peak gradually recovers. As shown in Fig. 7(d), most oxygen atoms in this region return to their original fcc sites, and most gallium atoms also reoccupy four- and six-coordinated sites, but with a coordination ratio of approximately 1:1.55, differing from the pristine β -phase ratio of 1:1. This ratio is more consistent with the experimentally reported value of 1:1.35 for the γ -phase structure [49].

Beyond the γ -phase region, a deformed β -phase structure is identified. Although the deformation is not readily apparent in the transverse view [Fig. 7(a)], it becomes evident from the RDFs and the atomic-displacement distributions. Specifically, Fig. 7(d) shows an overall shift of both oxygen and gallium displacement distributions in region III relative to the pristine β -phase lattice sites (region IV), while the widths of these distributions remain comparable. This indicates that region III retains the β -phase structure but experiences deformation induced by the ion track. Such deformation has also been observed in our TEM characterizations and is found to significantly influence the electronic properties of the β phase; these results will be reported elsewhere.

One of the central controversies in recent SHI irradiation experiments on β - Ga_2O_3 concerns the crystallinity of the ion tracks. Xu *et al.* [45] reported that the tracks are fully amorphous, whereas Abdullaev *et al.* [34] concluded that the tracks consist predominantly of the γ

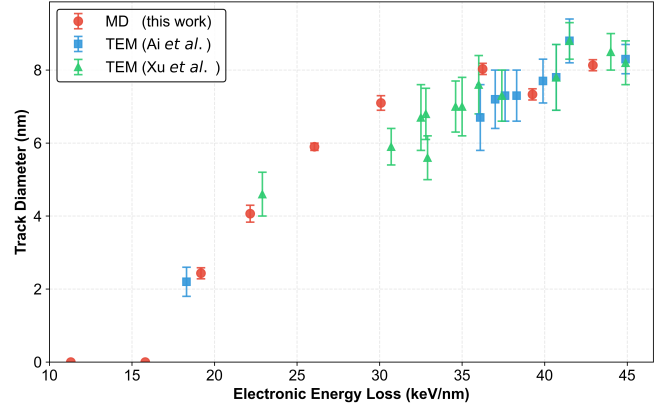


Figure 9. Comparison of the track diameters predicted in this work and the TEM results reported by Xu *et al.* [45] and Ai *et al.* [46].

phase. It is noteworthy that the samples studied by Abdullaev *et al.* were irradiated with a relatively low S_e of approximately 21 keV/nm, whereas most samples examined by Xu *et al.* were subjected to higher electronic energy losses exceeding 30 keV/nm. This difference in S_e may therefore provide a natural explanation for the seemingly conflicting experimental conclusions. However, Xu *et al.* also reported amorphous tracks at energy losses close to 20 keV/nm, which appears difficult to reconcile directly with the results of Abdullaev *et al.* This situation motivates a systematic investigation of SHI irradiation over a wide range of S_e . To this end, we performed a series of SHI irradiation simulations with S_e ranging from 11.29 to 42.92 keV/nm and five representative cases are

shown in Fig. 8.

When $S_e = 15.68$ keV/nm, no ion track is formed, consistent with the experimental threshold of approximately 17 keV/nm reported by Xu *et al.* [45]. The oxygen sub-lattice remains largely intact and defect-free, in agreement with previous theoretical predictions [26]. Only a small number of gallium interstitials are generated, most of which occupy four- or six-coordinated sites within the FCC oxygen framework. Such defect configurations can be regarded as incipient signatures of γ -phase formation. When S_e increases to 19.18 keV/nm, slightly above the experimental threshold, continuous γ -phase regions are observed in the both transverse and longitudinal cross-sectional views, with limited number of oxygen defects emerging. The simulated diffraction patterns for this case [Fig. S2] reproduce the key features observed experimentally [34], confirming the formation of γ -phase ion tracks at S_e slightly above the threshold.

At $S_e = 22.16$ keV/nm, corresponding to the energy-loss regime where the most controversial experimental interpretations have been reported, a clear core-shell track structure emerges. The shell consists predominantly of a well-defined γ phase, while the core forms a highly disordered region. Notably, although this core region is highly disordered, it is not fully amorphous. A substantial fraction of oxygen atoms remain distributed around their pristine FCC sites, albeit with large displacements. This quasi-FCC oxygen framework partially constrains the displacement of gallium atoms. Along the ion penetration direction, the thicknesses of the core and shell fluctuate heavily, and in some segments the disordered core even disappears, resulting in a track composed entirely of the γ phase. These observations suggest that this highly disordered core should be interpreted as a precursor state of the γ phase, which may transform into a standard γ structure under mild post-irradiation conditions, such as long-term defect relaxation at ambient conditions or TEM-induced structural recovery.

When S_e further increases to 26.05 keV/nm, the track size increases rapidly to approximately 6 nm in diameter. In this regime, the track core becomes fully amorphous, exhibiting no recognizable structural motifs. Compared with the case at $S_e = 22.16$ keV/nm, fluctuations along the ion penetration direction are strongly suppressed, indicating the formation of a continuous amorphous core and a stable core-shell structure. At $S_e = 36.24$ keV/nm, the track size increases further, with the track diameter reaching approximately 8 nm, while the core-shell morphology remains evident. Interestingly, the thickness of the surrounding γ -phase shell does not increase with increasing track size and saturates at about 1 nm.

To validate our simulation results, we compared the predicted track diameters with experimental measurements reported in Refs. [45, 46], as shown in Fig. 9. The figure includes simulation results for nine different values of S_e , with each case repeated three times to reduce statistical fluctuations in the MD simulations. All simulated transverse cross-sectional views, along with the

corresponding measured track diameters, are presented in Fig. S3 and Fig. S4. The simulated track diameter increases rapidly once S_e exceeds a threshold of approximately 17 keV/nm, whereas the growth rate decreases markedly when S_e exceeds 30 keV/nm. At even higher S_e , the monotonic dependence of the simulated track size on S_e becomes less evident, which we attribute to subtle differences in the electronic cascade kinetics induced by ions of different energies and species. The excellent agreement between simulation and experiment across a wide range of S_e demonstrates the reliability of our NEP model. Besides, the total computational throughput for these results exceeds 1.2×10^{13} atom-steps. Achieving the same throughput with tabGAP would require more than 69 days on eight CPU nodes, each equipped with two 24-core Intel Xeon Gold 6240R processors, whereas the computational time for NEP is estimated to be less than three days on a GPU cluster with four NVIDIA GeForce RTX 4090 GPUs. These results further highlight the suitability of NEP for high-throughput, large-scale MD simulations.

IV. CONCLUSION

In conclusion, by combining the NEP architecture with an energy-dependent weighting strategy, we develop a robust, accurate, and computationally efficient MLIP for Ga_2O_3 , which demonstrates clear and comprehensive advantages over the state-of-the-art tabGAP potential. Furthermore, by adopting a physically process-oriented sampling strategy, the NEP model trained on the augmented dataset is successfully applied to SHI irradiation simulations of $\beta\text{-Ga}_2\text{O}_3$. The simulated results are in quantitative agreement with experimental observations and provide a consistent and reliable physical explanation for the reported experimental discrepancies. In addition, the impressive computational efficiency of NEP enables large-scale MD simulations approaching the device scale for Ga_2O_3 systems [50]. This capability opens a new avenue for device-scale design and optimization of Ga_2O_3 -based devices from an atomistic simulation perspective.

ACKNOWLEDGMENTS

The authors acknowledge the National Natural Science Foundation of China (Grant No. 12325511), the Huizhou Science and Technology Talent Project (Grant No. 2024EQ050015), the Gansu Provincial Science and Technology Innovation Talent Program (Grant No. 24RCKB011), the Dongjiang Yuan Intelligent Computing Center for providing computational resources. The authors also thanks the valuable comments and suggestions from Jiaming Zhang and Wentao Wang.

Appendix A: Methodology of TREKIS

The central parameter in TREKIS is the differential scattering cross-section σ , which describes the interactions between ballistic electrons and orbital electrons. This parameter is calculated using the DSF-CDF formalism, based on optical data obtained from photoabsorption experiments:

$$\frac{\partial^2 \sigma}{\partial(\hbar\omega)\partial(\hbar q)} = \frac{2[Z_e(v, q)e]^2}{\pi\hbar^2 v^2} \frac{1}{\hbar q} \text{Im}\left[\frac{-1}{\epsilon(\omega, q)}\right], \quad (\text{A1})$$

In this formalism, $\hbar\omega$ represents the transferred energy, q denotes the transferred momentum, v is the ion velocity, Z_e is the effective charge of the ion passing through Ga_2O_3 , and ϵ is the complex dielectric function. The ion charge $Z_e(v, q)$ is calculated with Barkas formula [51]:

$$Z_e(v, q) = Z_{\text{ion}}(1 - \exp(-\frac{v}{v_0} Z_{\text{ion}}^{-\frac{2}{3}})) \quad (\text{A2})$$

where v is the velocity of the ion, $v_0 = c/125$ is the empirical atomic electron velocity and Z_{ion} is the ion charge in full ionization. The optical energy loss function of Ga_2O_3 is taken from Ref. [6], and fitted with a finite sum of Drude-Lorentz oscillator functions:

$$\text{Im}\left(\frac{-1}{\epsilon(\omega, 0)}\right) = \sum_i \frac{A_i \gamma_i \hbar\omega}{(\hbar^2 \omega^2 - E_i^2)^2 + (\gamma_i \hbar\omega)^2} \quad (\text{A3})$$

where A_i , γ_i , and E_i are the fitted parameters, which are constrained by two sum rules:

1. The f-sum rule:

$$\frac{2}{\pi \Omega_p^2} \int_{I_p}^{\infty} \text{Im}\left(\frac{-1}{\epsilon(\omega, 0)}\right)_{\text{shell}} \omega d\omega = N_{e,\text{shell}} \quad (\text{A4})$$

where $\Omega_p^2 = 4\pi e^2 n_{at}/m_e$ is the plasma frequency, $N_{e,\text{shell}}$ is the number of electrons in selected shell, and I_p is ionization potential.

2. The KK-sum rule:

$$\frac{2}{\pi} \int_0^{\infty} \text{Im}\left(\frac{-1}{\epsilon(\omega, 0)}\right) \frac{d\omega}{\omega} = 1 \quad (\text{A5})$$

The free-electron approximation is used to calculate the dispersion relation for the oscillator energy E_i and transferred momentum q :

$$E_i(q) = E_i(0) + \frac{\hbar^2 q^2}{2m_e} \quad (\text{A6})$$

The lower and upper limits of the transferred energy during an inelastic scattering event are as follows:

$$W_- = I_p \quad (\text{A7})$$

$$W_+ = \frac{4Em_1m_2}{(m_1 + m_2)^2} \quad (\text{A8})$$

where E is the incident energy, and m_1 and m_2 are the masses of the two scattering particles. For the elastic scattering between electrons and atoms, i.e., the electron-phonon interaction, the Mott scattering cross section is employed with a modified Molière screening parameter K_{scr} [52], given by the following equation:

$$\sigma_{\text{elastic}} = \sigma_{\text{Mott}} K_{\text{scr}} \quad (\text{A9})$$

The upper limit of transferred energy in the elastic scattering event is:

$$W_+ = \min\left(\frac{4Em_1m_2}{(m_1 + m_2)^2}, \hbar\omega_{\text{Debye}}\right) \quad (\text{A10})$$

where $\omega_{\text{Debye}} = (6\pi^2 n_{at})^{\frac{1}{3}} v_s$ is the Debye frequency and v_s is the speed of sound in Ga_2O_3 .

Several additional parameters were incorporated into the TREKIS calculations: the speed of sound was set to 5,250 m/s [53], the density of Ga_2O_3 to 5.88 g/cm³, and the band gap to 4.9 eV [54].

Appendix B: Technical details for MD simulations

All MD simulations of SHI irradiation on $\beta\text{-Ga}_2\text{O}_3$ were performed using GPUMD. The simulations were initialized with a $\beta\text{-Ga}_2\text{O}_3$ lattice configuration oriented with the [010] crystallographic direction (y -axis) aligned along the ion penetration direction. Each simulation ran for a total of 200 ps in the NVE ensemble, with boundary temperature controlled using Nose-Hoover chain thermostats with coupling parameters tuned to 1,000. The time step was dynamically adjusted to mitigate instabilities arising from extreme temperature gradients: 0.25 fs for the initial 10 ps, 0.5 fs for the subsequent 90 ps, and 1 fs for the final 100 ps. To minimize boundary effects, the simulation cell was constructed with dimensions of $38.8 \times 10.5 \times 39.5$ nm, containing 1,457,920 atoms in total. To verify the sufficiency of the cell thickness, we also tested a model with dimensions of $38.8 \times 21.0 \times 39.5$ nm and found no significant difference in the final results between the standard and doubled-thickness models.

[1] S. J. Pearton, J. Yang, P. H. Cary, F. Ren, J. Kim, M. J. Tadjer, and M. A. Mastro, A review of Ga_2O_3 materials, processing, and devices, *Appl. Phys. Rev.* **5**, 011301 (2017).

[2] M. J. Tadjer, Toward gallium oxide power electronics, *Science* **378**, 724 (2022).

[3] A. S. Pratiyush, S. Krishnamoorthy, R. Muralidharan, S. Rajan, and D. N. Nath, Advances in Ga_2O_3 solar-blind uv photodetectors, in *Gallium Oxide* (Elsevier, 2019) pp. 369–399.

[4] J. Zhu, Z. Xu, S. Ha, D. Li, K. Zhang, H. Zhang, and J. Feng, Gallium Oxide for Gas Sensor Applications: A Comprehensive Review, *Materials* **15**, 7339 (2022).

[5] S. Yoshioka, H. Hayashi, A. Kuwabara, F. Oba, K. Matsunaga, and I. Tanaka, Structures and energetics of Ga_2O_3 polymorphs, *J. Phys.: Condens. Matter* **19**, 346211 (2007).

[6] H. He, R. Orlando, M. A. Blanco, R. Pandey, E. Amzallag, I. Baraille, and M. Rérat, First-principles study of the structural, electronic, and optical properties of Ga_2O_3 in its monoclinic and hexagonal phases, *Phys. Rev. B* **74**, 195123 (2006).

[7] J. Xu, J. Zhai, and X. Yao, Structure and dielectric properties of barium titanate thin films grown by sol-gel-hydrothermal process, *Appl. Phys. Lett.* **89**, 252902 (2007).

[8] J. B. Varley, J. R. Weber, A. Janotti, and C. G. Van De Walle, Oxygen vacancies and donor impurities in β - Ga_2O_3 , *Appl. Phys. Lett.* **97**, 142106 (2010).

[9] Z. Yan and S. Kumar, Phonon mode contributions to thermal conductivity of pristine and defective β - Ga_2O_3 , *Phys. Chem. Chem. Phys.* **20**, 29236 (2018).

[10] J. Yang, Y. Xu, X. Wang, X. Zhang, Y. He, and H. Sun, Lattice thermal conductivity of β -, α - and κ - Ga_2O_3 : a first-principles computational study, *Appl. Phys. Express* **17**, 011001 (2024).

[11] V. Bermudez, The structure of low-index surfaces of β - Ga_2O_3 , *Chem. Phys.* **323**, 193 (2006).

[12] Q. Fan, R. Zhao, W. Zhang, Y. Song, M. Sun, and U. Schwingenschlögl, Low-energy Ga_2O_3 polymorphs with low electron effective masses, *Phys. Chem. Chem. Phys.* **24**, 7045 (2022).

[13] A. Azarov, C. Baziotti, V. Venkatachalam, P. Vajeston, E. Monakhov, and A. Kuznetsov, Disorder-Induced Ordering in Gallium Oxide Polymorphs, *Phys. Rev. Lett.* **128**, 015704 (2021).

[14] X. Han, Y. Liu, Y. Li, M. L. Crespillo, E. Zarkadoula, W. Mu, and P. Liu, Unraveling the Atomic Mechanism of the Crystalline Phase-Dependent Structural Features and Special Spectral Design of α -, β -, and ϵ - Ga_2O_3 , *Adv. Sci.* **12**, e08207 (2025).

[15] M. A. Blanco, M. B. Sahariah, H. Jiang, A. Costales, and R. Pandey, Energetics and migration of point defects in Ga_2O_3 , *Phys. Rev. B* **72**, 184103 (2005).

[16] E. O. Pyzer-Knapp, J. W. Pitera, P. W. J. Staar, S. Takeda, T. Laino, D. P. Sanders, J. Sexton, J. R. Smith, and A. Curioni, Accelerating materials discovery using artificial intelligence, high performance computing and robotics, *npj Comput. Mater.* **8**, 84 (2022).

[17] T. W. Ko and S. P. Ong, Recent advances and outstanding challenges for machine learning interatomic potentials, *Nat. Comput. Sci.* **3**, 998 (2023).

[18] R. Li, Z. Liu, A. Rohskopf, K. Gordiz, A. Henry, E. Lee, and T. Luo, A deep neural network interatomic potential for studying thermal conductivity of β - Ga_2O_3 , *Appl. Phys. Lett.* **117**, 152102 (2020).

[19] Y.-B. Liu, J.-Y. Yang, G.-M. Xin, L.-H. Liu, G. Csányi, and B.-Y. Cao, Machine learning interatomic potential developed for molecular simulations on thermal properties of β - Ga_2O_3 , *J. Chem. Phys.* **153**, 144501 (2020).

[20] J. Zhao, J. Byggmästar, Z. Zhang, F. Djurabekova, K. Nordlund, and M. Hua, Phase transition of two-dimensional ferroelectric and paraelectric Ga_2O_3 monolayers: A density functional theory and machine learning study, *Phys. Rev. B* **104**, 054107 (2021).

[21] Z. Sun, Z. Qi, K. Liang, X. Sun, Z. Zhang, L. Li, Q. Wang, G. Zhang, G. Wu, and W. Shen, A neuroevolution potential for predicting the thermal conductivity of α - Ga_2O_3 , β - Ga_2O_3 , and ϵ - Ga_2O_3 , *Appl. Phys. Lett.* **123**, 192202 (2023).

[22] X. Wang, J. Yang, P. Ying, Z. Fan, J. Zhang, and H. Sun, Dissimilar thermal transport properties in κ - Ga_2O_3 and β - Ga_2O_3 revealed by homogeneous nonequilibrium molecular dynamics simulations using machine-learned potentials, *J. Appl. Phys.* **135**, 065104 (2024).

[23] Y. Liu, H. Liang, L. Yang, G. Yang, H. Yang, S. Song, Z. Mei, G. Csányi, and B. Cao, Unraveling Thermal Transport Correlated with Atomistic Structures in Amorphous Gallium Oxide via Machine Learning Combined with Experiments, *Adv. Mater.* **35**, 2210873 (2023).

[24] J. Zhao, J. Byggmästar, H. He, K. Nordlund, F. Djurabekova, and M. Hua, Complex Ga_2O_3 polymorphs explored by accurate and general-purpose machine-learning interatomic potentials, *npj Comput. Mater.* **9**, 159 (2023).

[25] H. He, J. Zhao, J. Byggmästar, R. He, K. Nordlund, C. He, and F. Djurabekova, Threshold displacement energy map of Frenkel pair generation in β - Ga_2O_3 from machine-learning-driven molecular dynamics simulations, *Acta Mater.* **276**, 120087 (2024).

[26] R. He, J. Zhao, J. Byggmästar, H. He, and F. Djurabekova, Ultrahigh stability of oxygen sublattice in β - Ga_2O_3 , *Phys. Rev. Materials* **8**, 084601 (2024).

[27] T. Liu, Z. Li, J. Zhao, X. Fei, J. Feng, Y. Zuo, M. Hua, Y. Guo, S. Liu, and Z. Zhang, Orientation-dependent surface radiation damage in β - Ga_2O_3 explored by atomistic simulations, *Acta Mater.* **300**, 121484 (2025).

[28] A. Azarov, C. Radu, A. Galekas, I. F. Mercioniu, A. Cernescu, V. Venkatachalam, E. Monakhov, F. Djurabekova, C. Ghica, J. Zhao, and A. Kuznetsov, Self-Assembling of Multilayered Polymorphs with Ion Beams, *Nano Lett.* **25**, 1637 (2025).

[29] J. Zhang, J. Zhao, J. Chen, and M. Hua, Orientation-dependent atomic-scale mechanism and defect evolution in β - Ga_2O_3 thin film epitaxial growth, *Appl. Phys. Lett.* **124**, 022102 (2023).

[30] Q. Li, J. Zhao, N. Lin, X. Cheng, X. Zhao, Z. Liu, Z. Jia, and M. Hua, Edge-Dependent Step-Flow Growth Mechanism in β - Ga_2O_3 (100) Facet at the Atomic Level, *J. Phys. Chem. Lett.* **16**, 5101 (2025).

[31] A. Azarov, J. G. Fernández, J. Zhao, F. Djurabekova, H. He, R. He, Ø. Prytz, L. Vines, U. Bektaş, P. Chekhonin, N. Klingner, G. Hlawacek, and A. Kuznetsov, Universal radiation tolerant semiconductor, *Nat. Commun.* **14**, 4855 (2023).

[32] J. Zhao, J. G. Fernández, A. Azarov, R. He, Ø. Prytz, K. Nordlund, M. Hua, F. Djurabekova, and A. Kuznetsov, Crystallization Instead of Amorphization in Collision Cascades in Gallium Oxide, *Phys. Rev. Lett.* **134**, 126101 (2025).

[33] X. Han, Y. Li, M. L. Crespillo, E. Zarkadoula, Y. Liu, W. Mu, S. Zhao, and P. Liu, Electronic Excitation-Driven β -Ga₂O₃ Metastability Transformation and Self-Organization Mechanism: $\beta \rightarrow \kappa/\gamma/\delta$ Phases, *Adv. Mater.* , e19259 (2025).

[34] A. Abdullaev, J. G. Fernandez, C. Nozais, J. O'Connell, R. Tlegennov, K. Sekerbayev, A. Azarov, A. Leino, T. F. Bouvier, J. Zhao, A. A. Pena, N. Medvedev, Z. Utlegulov, O. Prytz, F. Djurabekova, and A. Kuznetsov, Ions leaving no tracks (2025), version Number: 2.

[35] K. Xu, H. Bu, S. Pan, E. Lindgren, Y. Wu, Y. Wang, J. Liu, K. Song, B. Xu, Y. Li, T. Hainer, L. Svensson, J. Wiktor, R. Zhao, H. Huang, C. Qian, S. Zhang, Z. Zeng, B. Zhang, B. Tang, Y. Xiao, Z. Yan, J. Shi, Z. Liang, J. Wang, T. Liang, S. Cao, Y. Wang, P. Ying, N. Xu, C. Chen, Y. Zhang, Z. Chen, X. Wu, W. Jiang, E. Berger, Y. Li, S. Chen, A. J. Gabourie, H. Dong, S. Xiong, N. Wei, Y. Chen, J. Xu, F. Ding, Z. Sun, T. Ala-Nissila, A. Harju, J. Zheng, P. Guan, P. Erhart, J. Sun, W. Ouyang, Y. Su, and Z. Fan, GPUMD 4.0: A high-performance molecular dynamics package for versatile materials simulations with machine-learned potentials, *Mater. Genome Eng. Adv.* **3**, e70028 (2025).

[36] Z. Fan, Z. Zeng, C. Zhang, Y. Wang, K. Song, H. Dong, Y. Chen, and T. Ala-Nissila, Neuroevolution machine learning potentials: Combining high accuracy and low cost in atomistic simulations and application to heat transport, *Phys. Rev. B* **104**, 104309 (2021).

[37] Z. Fan, Y. Wang, P. Ying, K. Song, J. Wang, Y. Wang, Z. Zeng, K. Xu, E. Lindgren, J. M. Rahm, A. J. Gabourie, J. Liu, H. Dong, J. Wu, Y. Chen, Z. Zhong, J. Sun, P. Erhart, Y. Su, and T. Ala-Nissila, GPUMD: A package for constructing accurate machine-learned potentials and performing highly efficient atomistic simulations, *J. Chem. Phys.* **157**, 114801 (2022).

[38] K. Song, R. Zhao, J. Liu, Y. Wang, E. Lindgren, Y. Wang, S. Chen, K. Xu, T. Liang, P. Ying, N. Xu, Z. Zhao, J. Shi, J. Wang, S. Lyu, Z. Zeng, S. Liang, H. Dong, L. Sun, Y. Chen, Z. Zhang, W. Guo, P. Qian, J. Sun, P. Erhart, T. Ala-Nissila, Y. Su, and Z. Fan, General-purpose machine-learned potential for 16 elemental metals and their alloys, *Nat. Commun.* **15**, 10208 (2024).

[39] T. Liang, K. Xu, E. Lindgren, Z. Chen, R. Zhao, J. Liu, E. Berger, B. Tang, B. Zhang, Y. Wang, K. Song, P. Ying, N. Xu, H. Dong, S. Chen, P. Erhart, Z. Fan, T. Ala-Nissila, and J. Xu, NEP89: Universal neuroevolution potential for inorganic and organic materials across 89 elements (2025), arXiv:2504.21286 [cond-mat].

[40] R. A. Rymzhanov, N. Medvedev, and A. E. Volkov, Damage threshold and structure of swift heavy ion tracks in Al₂O₃, *J. Phys. D: Appl. Phys.* **50**, 475301 (2017).

[41] N. A. Medvedev, R. A. Rymzhanov, and A. E. Volkov, Time-resolved electron kinetics in swift heavy ion irradiated solids, *J. Phys. D: Appl. Phys.* **48**, 355303 (2015).

[42] R. Rymzhanov, N. Medvedev, and A. Volkov, Effects of model approximations for electron, hole, and photon transport in swift heavy ion tracks, *Nucl. Instrum. Methods Phys. Res., Sect. B* **388**, 41 (2016).

[43] B. Deng, Y. Choi, P. Zhong, J. Riebesell, S. Anand, Z. Li, K. Jun, K. A. Persson, and G. Ceder, Systematic softening in universal machine learning interatomic potentials, *npj Comput. Mater.* **11**, 9 (2024).

[44] C. Chen, Y. Li, R. Zhao, Z. Liu, Z. Fan, G. Tang, and Z. Wang, NepTrain and NepTrainKit: Automated Active Learning and Visualization Toolkit for Neuroevolution Potentials (2025), arXiv:2506.01868 [cs].

[45] L. Xu, P. Zhai, P. Hu, S. Zhang, J. Zeng, Z. Li, W. Li, M. E. Toimil-Molares, C. Trautmann, and J. Liu, Thermal stability of swift heavy ion tracks in β -Ga₂O₃ annealed at high temperatures, *Appl. Phys. Lett.* **127**, 151903 (2025).

[46] W. Ai, L. Xu, S. Nan, P. Zhai, W. Li, Z. Li, P. Hu, J. Zeng, S. Zhang, L. Liu, Y. Sun, and J. Liu, Radiation damage in β -Ga₂O₃ induced by swift heavy ions, *Jpn. J. Appl. Phys.* **58**, 120914 (2019).

[47] L. E. Ratcliff, T. Oshima, F. Nippert, B. M. Janzen, E. Kluth, R. Goldhahn, M. Feneberg, P. Mazzolini, O. Bierwagen, C. Wouters, M. Nofal, M. Albrecht, J. E. N. Swallow, L. A. H. Jones, P. K. Thakur, T. Lee, C. Kalha, C. Schlueter, T. D. Veal, J. B. Varley, M. R. Wagner, and A. Regoutz, Tackling Disorder in γ -Ga₂O₃, *Adv. Mater.* **34**, 2204217 (2022).

[48] Q.-S. Huang, C.-N. Li, M.-S. Hao, H.-P. Liang, X. Cai, Y. Yue, A. Kuznetsov, X. Zhang, and S.-H. Wei, Nature of Disordering in γ -Ga₂O₃, *Phys. Rev. Lett.* **133**, 226101 (2024).

[49] H. Y. Playford, A. C. Hannon, E. R. Barney, and R. I. Walton, Structures of Uncharacterised Polymorphs of Gallium Oxide from Total Neutron Diffraction, *Chem. - Eur. J.* **19**, 2803 (2013).

[50] K. Xu, G. Wang, T. Liang, Y. Xiao, D. Ding, H. Guo, X. Gao, L. Tong, X. Wan, G. Zhang, and J. Xu, Device-Scale Atomistic Simulations of Heat Transport in Advanced Field-Effect Transistors (2025), arXiv:2511.18915 [cond-mat].

[51] B. Gervais and S. Bouffard, Simulation of the primary stage of the interaction of swift heavy ions with condensed matter, *Nucl. Instrum. Methods Phys. Res., Sect. B* **88**, 355 (1994).

[52] T. M. Jenkins, W. R. Nelson, and A. Rindi, *Monte Carlo transport of electrons and photons*, Vol. 38 (Springer Science & Business Media, 2012).

[53] D. Wright, E. Guzman, M. S. H. Bijoy, R. B. Wilson, D. H. Mudiyanselage, H. Fu, F. Kargar, and A. A. Balandin, Acoustic phonon characteristics of (001) and $(\bar{2}01)$ β -Ga₂O₃ single crystals investigated with brillouin-mandelstam light scattering spectroscopy (2025).

[54] Y. Zhang, M. Liu, D. Jena, and G. Khalsa, Tight-binding band structure of β - and α -phase Ga₂O₃ and Al₂O₃, *J. Appl. Phys.* **131**, 175702 (2022).

**Supplemental Material for
“A Neuroevolution Potential for Gallium Oxide:
Accurate and Efficient Modeling of Polymorphism and Swift Heavy-Ion Irradiation”**

Yaohui Gu,^{1,2} Binbo Li,^{1,2,*} Linyang Jiang,^{1,2} Yuhui Hu,^{1,2,3} Wenqiang Liu,^{1,2} Lijun Xu,^{1,2} Pengfei Zhai,^{1,2} Jie Liu,^{1,2} and Jinglai Duan^{1,2,4,†}

¹*State Key Laboratory of Heavy Ion Science and Technology,*

Institute of Modern Physics, Chinese Academy of Sciences, Lanzhou 730000, China

²*School of Nuclear Science and Technology, University of Chinese Academy of Sciences, Beijing 100049, China*

³*School of Materials & Energy, Lanzhou University, Lanzhou, 730000, China*

⁴*Advanced Energy Science and Technology Guangdong Laboratory, Huizhou 516000, China*

(Dated: January 16, 2026)

I. EXTRA FIGURES

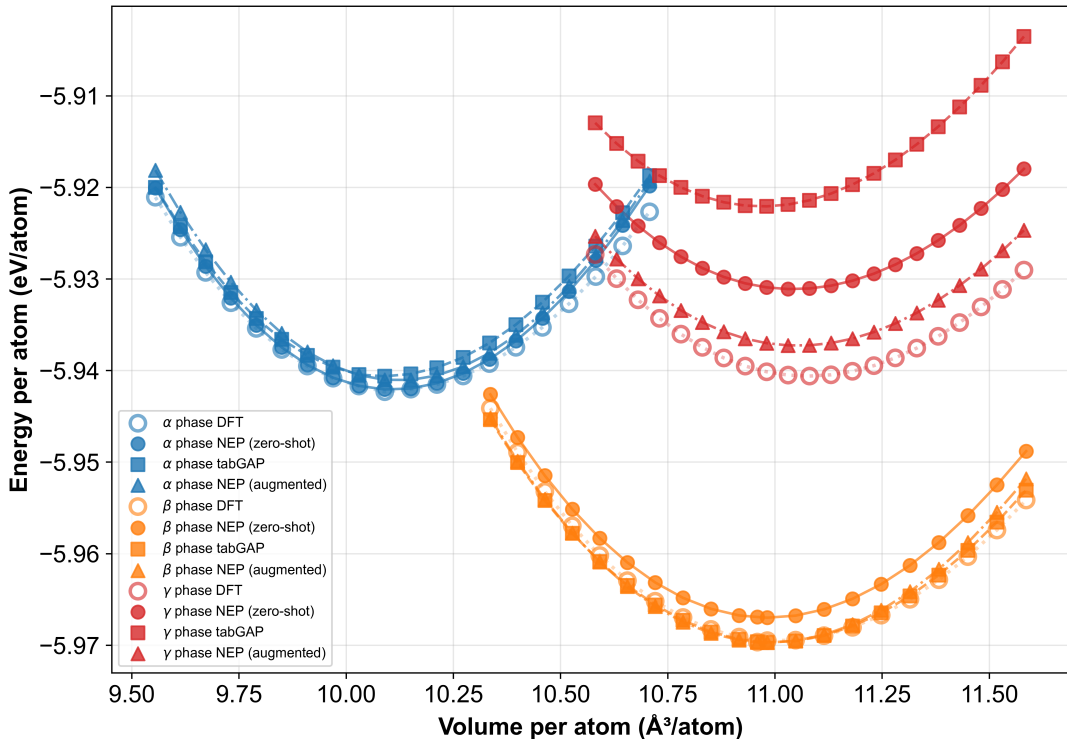


FIG. S1. Energy-volume curves for the α , β and γ phases predicted by zero-shot NEP (solid circles), NEP with augmented training set (solid triangles), and tabGAP (solid squares), compared with DFT reference data (open circles). Different phases are color-coded as indicated.

* Y.G. and B.L. contributed equally to this work.

† Corresponding author. Email: j.duan@impcas.ac.cn

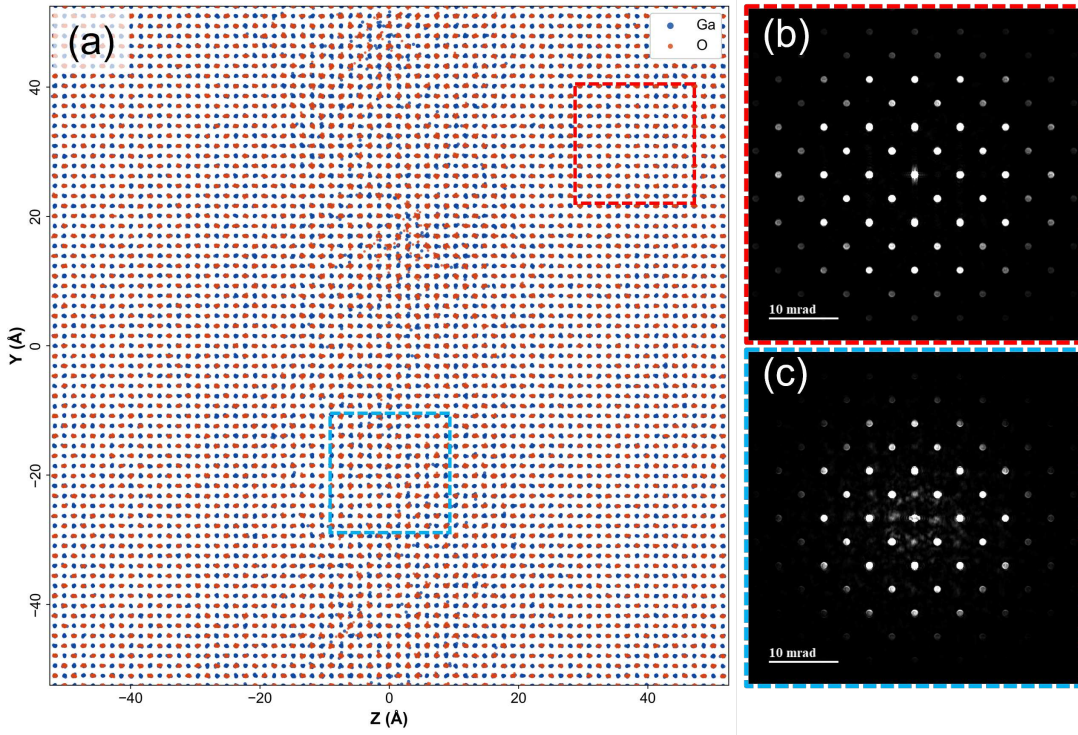


FIG. S2. (a) Longitudinal cross-sectional view of the SHI-irradiated β - Ga_2O_3 atomic structure with $S_e = 19.18$ keV/nm, the vertical direction is along [201] direction. (b) Simulated diffraction pattern for the pristine β phase. (c) Simulated diffraction pattern for the γ phase.

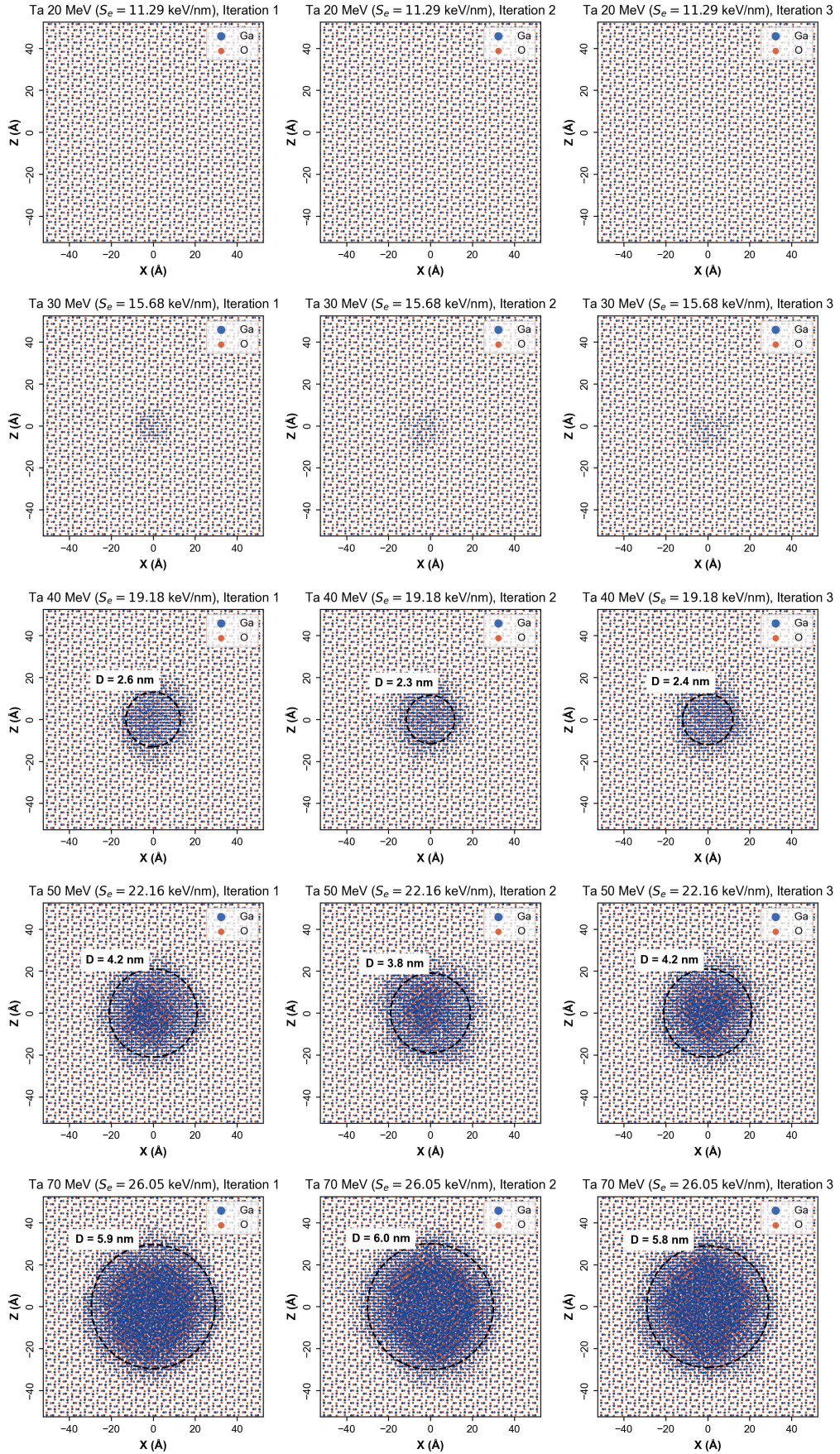


FIG. S3. Transverse cross-sectional views of ion tracks in β -Ga₂O₃ for electronic energy losses ranging from $S_e = 11.29$ keV/nm to $S_e = 26.05$ keV/nm. The measured track diameters are indicated for each case.

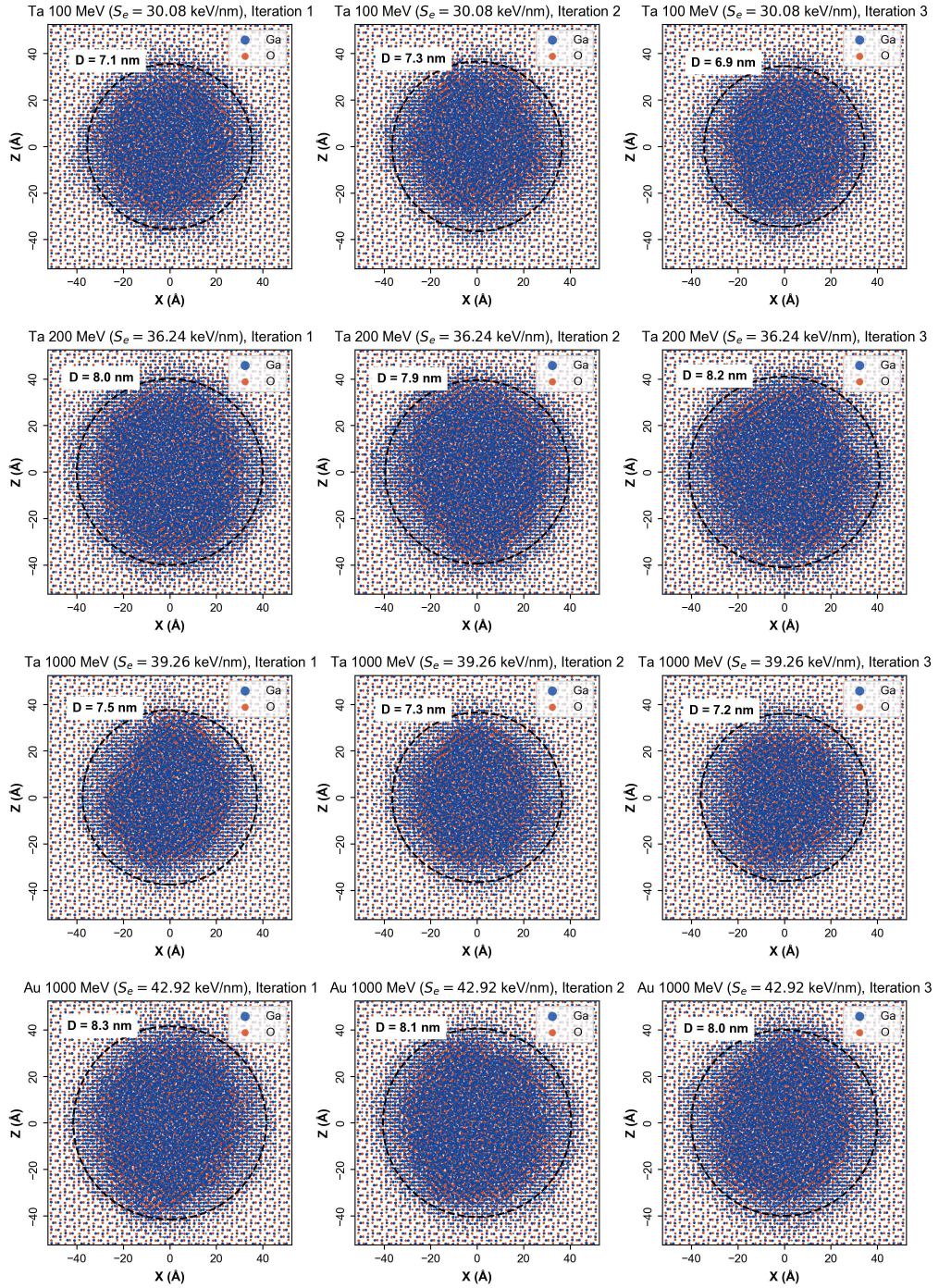


FIG. S4. Transverse cross-sectional views of ion tracks in β -Ga₂O₃ for electronic energy losses ranging from $S_e = 30.08$ keV/nm to $S_e = 42.92$ keV/nm. The measured track diameters are indicated for each case.